

Design of TE and TM Mode Mach-Zehnder Interferometer based on SOI Technology

Sourangsu Banerji,

Department of Electronics & Communication Engineering,
RCC-Institute of Information Technology

Abstract—Mach-Zehnder Interferometer (MZI) is one of the most important building blocks in photonic circuits. They are extensively used in modulators, optical filters, WDM multiplexers, photonic biosensors etc. In this project report, we will study simple non-modulated MZI devices for both TE and TM mode of operation in order to explain the theory of MZI operation and compare simulation and test results of such fabricated MZI devices.

Index Terms—Mach-Zehnder Interferometer, SOI Technology, TE Mode, TM Mode, Waveguide

I. INTRODUCTION

A critical role is anticipated to be played by silicon nanophotonics in future ultra-compact system integration due to the maturity of silicon complementary metal-oxide-semiconductor (CMOS) technology. Silicon is transparent in the range of optical telecommunication wavelengths, and it has high refractive index that allows for the fabrication of high-index-contrast nano-photonics structures. In this report, we demonstrate the design of a simple Mach Zehnder Interferometer. The device will be fabricated using Silicon over Insulator (SOI) technology.

Mach-Zehnder Interferometers are commonly employed in telecommunications applications such as switches, modulators and filters [1-7]. In certain biosensing applications, MZIs are commonly used to allow one of the arms of an interferometer to interact with an analyte via a waveguides' evanescent field. In this report simulations in terms of optical components using Lumerical Mode Solutions and MATLAB as well as circuit level simulations using Lumerical Interconnect have been shown, which later on will be compared with experimental results after the device have been fabricated.

II. THEORY

A. Working Principle of a Mach-Zehnder Interferometer

The Mach-Zehnder interferometer uses two separate beam splitters to split and recombine the beams, and has two outputs, which can be sent to the photodetectors. The path lengths in the two arms may be nearly identical (as shown in fig.1), or may be different (with an extra delay line). The distribution of optical powers at the two outputs depends on the accurate difference in optical arm lengths and on the wavelength (optical frequency). In a well aligned interferometer structure, the path length difference can be adjusted by slightly moving one of the mirrors so that for a particular optical frequency the total power goes into one of the outputs. However, for

misaligned beams (with one mirror being slightly tilted), there will be some fringe patterns in both outputs, and variations of the path length difference affect mainly the shapes of these interference patterns, whereas the distribution of total powers on the outputs may not change very much [2].

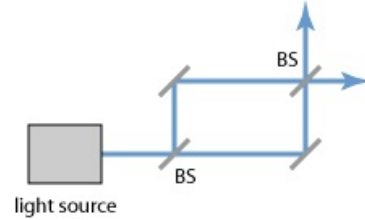


Fig. 1: Mach Zehnder Interferometer

B. Basic operation of a Mach-Zehnder Interferometer

In this report, a brief theoretical explanation of the operation of a Mach-Zehnder interferometer is given in terms of their gain spectrum response. The model used here, mainly applies to single-mode waveguides, where the total field intensity within each waveguide is considered unlike the field distribution inside the waveguides.

Let us consider the input intensity to be I_i , with an associated electric field of E_i . At the output of the first Y-branch, the value of the electric field at both the branches are given as $E_1 = \frac{E_i}{\sqrt{2}}$ and $E_2 = \frac{E_i}{\sqrt{2}}$. The propagation of light $\beta_1 = \frac{2\pi n_1}{\lambda}$ and $\beta_2 = \frac{2\pi n_2}{\lambda}$ in each of the waveguides is characterized by the expression,. The length of each waveguide is given as L_1 and L_2 , where $L_2 = L_1 + \Delta L$. The propagation loss is given by α_1 and α_2 for each of the respective individual waveguides. At the end of the two waveguides, the fields are:

$$E_{o1} = E_1 e^{-i\beta_1 L_1 - \frac{\alpha_1}{2} L_1} = \frac{E_i}{\sqrt{2}} e^{-i\beta_1 L_1 - \frac{\alpha_1}{2} L_1} \quad (1)$$

$$E_{o2} = E_2 e^{-i\beta_2 L_2 - \frac{\alpha_2}{2} L_2} = \frac{E_i}{\sqrt{2}} e^{-i\beta_2 L_2 - \frac{\alpha_2}{2} L_2} \quad (2)$$

The output of the Y branch combiner can be given as:

$$E_o = \frac{1}{\sqrt{2}} (E_{o1} + E_{o2}) = \frac{E_i}{2} (e^{-i\beta_1 L_1 - \frac{\alpha_1}{2} L_1} + e^{-i\beta_2 L_2 - \frac{\alpha_2}{2} L_2}) \quad (3)$$

Thus, the output intensity is:

$$I_o = \frac{I_i}{4} |e^{-i\beta_1 L_1 - \frac{\alpha_1}{2} L_1} + e^{-i\beta_2 L_2 - \frac{\alpha_2}{2} L_2}|^2 \quad (4)$$

To simplify our calculations, we assume that the total loss is negligible. In such cases, eqn.(4) simplifies to:

$$I_o = \frac{I_i}{4} [2 \cos(\frac{\beta_1 L_1 - \beta_2 L_2}{2})]^2 \quad (5)$$

$$I_o = I_i \cos^2(\frac{\beta_1 L_1 - \beta_2 L_2}{2}) \quad (6)$$

$$I_o = \frac{I_i}{2} [1 + \cos(\beta_1 L_1 - \beta_2 L_2)] \quad (7)$$

Thus, we can see that the interferometer's output is a sinusoidally varying function of wavelength (β_1 and β_2) for an imbalanced interferometer (L_1 not equals L_2) [2]. This period is termed as the free spectral range, and for identical waveguides, is determined by:

$$FSR[Hz] = \frac{c}{n_g \Delta L} \quad (8)$$

$$FSR[m] = \frac{\lambda^2}{n_g \Delta L} \quad (9)$$

III. MODELLING AND SIMULATION

The photonics component modelling was done in Lumerical Mode Solutions. A strip waveguide structure was chosen with the following dimensions:

Width = 500 nm and Height = 220 nm

In the model, we considered the x and y axes for the cross-section of the waveguide, and z for the length of the waveguide and propagation direction. The waveguide geometry consisted of SiO_2 (cladding material), for which the x-span as well as the y-span was set to $5\mu m$. For Si (core material), the x-span was taken as $0.5\mu m$, we define the y_{min} to be 0, which is the interface between the silicon and silicon dioxide, and 0.22 microns is our thickness of the waveguide i.e. y-span equals $0.22\mu m$. For both SiO_2 and Si , the z-span was taken as $0.6\mu m$. The refractive index of the materials was taken from Palik's Handbook of Optical Constants [6]. We had to add a simulation region i.e. eigenmode solver FDE to calculate the properties like mode profiles, the effective index, the group index etc. The x span was $3.5\mu m$, which leaves 1 micron on each side of the wave guide. The y span, was set to $2.55\mu m$ (for both quasi-TE and quasi-TM mode). The simulation region center was to be set to the middle of the waveguide, namely $0.11\mu m$. We changed the mesh settings to increase the number of mesh points to 250 in both the x and y direction to have more accurate simulations and better mode profile images. The boundary conditions were set to the default, namely metallic. The eigenmode solver type was 2D Z-normal.

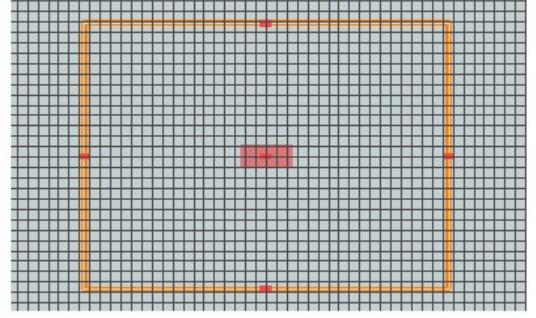


Fig. 2: Waveguide geometry in Lumerical MODE Solutions

A. Modal Analysis

The wavelength which was taken up in the modal analysis was set to $1.5\mu m$. Then, we meshed the structure to check if the meshing was done correctly, otherwise there would be error in our simulations. The number of trial modes was set to 20 and the search was made near the refractive index value of $n=3.47998$. Fig.3 (a) and (b) shows the mode profile for the quasi-TE mode of the waveguide in both the linear and log scale. Here we see that the electric field intensity is mostly confined within the waveguide. The log scale plot of the mode profile shows that the electric field has decayed in both the x and y directions and hence, we can say that the metal boundary is not interfering with the field in any of the directions. Similarly, fig.4 (a) and (b) shows the mode profile in both linear and log scales for the quasi-TM Mode where most of electric field intensity is outside the waveguide unlike the quasi-TE case.

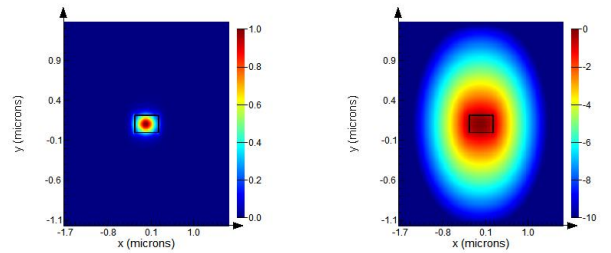


Fig. 3: Mode profile of straight waveguide (500 nm x 220 nm) for quasi-TE mode: (a) Electric field intensity (Linear scale) (b) Electric field intensity (Log scale)

B. Frequency Analysis

The start and stop wavelength for the frequency analysis was taken to be $1.5\mu m$ and $1.6\mu m$ respectively. The number of wavelength sweeps performed were 10 and the number of modes was taken to be 1 since, we required only the group index for the fundamental mode. We opted for a detailed dispersion calculation. Fig.5 and fig.6 depicts the plots of effective index versus wavelength and the group index versus wavelength respectively for the quasi-TE mode. From the plot of group index versus wavelength, the effective group index was found out to be 4.192 which can be approximated to 4.2.

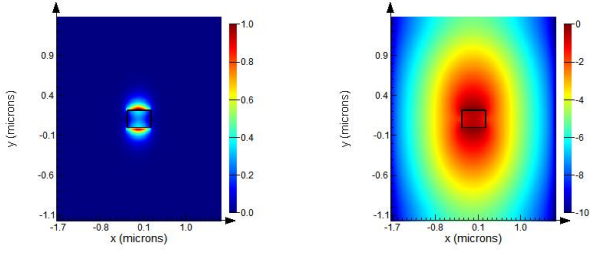


Fig. 4: Mode profile of straight waveguide (500 nm x 220 nm) for quasi-TM mode: (a) Electric field intensity (Linear scale) (b) Electric field intensity (Log scale)

The effective index was calculated to be 2.444347. In the plot, a complex refractive index was taken but in our model, we are only interested in the real part ignoring the complex part. Similarly, Fig.7 and fig.8 shows the frequency analysis for the quasi-TM Mode, the effective group index was found out to be 3.721 which can be approximated to 3.7. The effective index was calculated to be 1.838867.

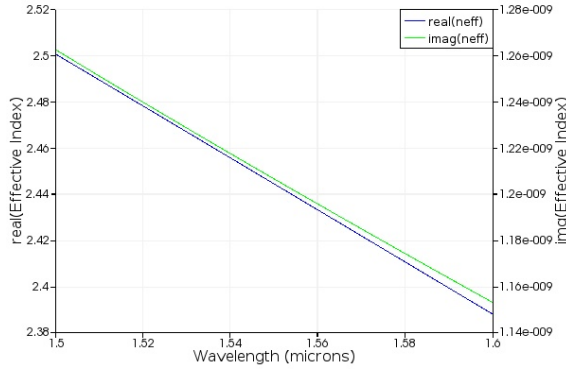


Fig. 5: Effective Index (n_{eff}) for quasi-TE mode

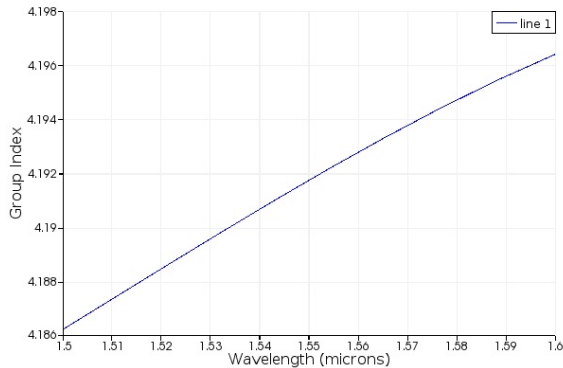


Fig. 6: Group Index (n_g) for quasi-TE mode

C. Compact Waveguide Model

After using the Lumerical Mode Solutions to extract effective index information for both the quasi-TE and quasi-TM mode of the waveguide, the next step is to get a model

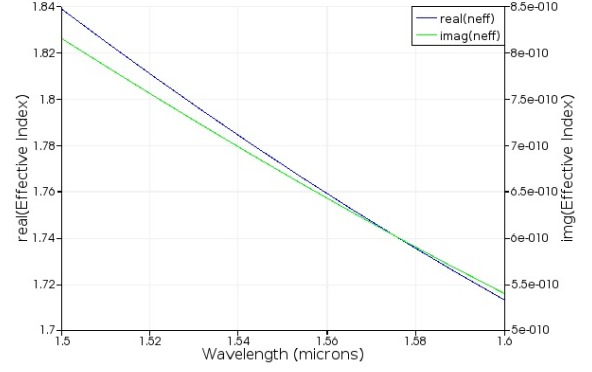


Fig. 7: Effective Index (n_{eff}) for quasi-TM mode

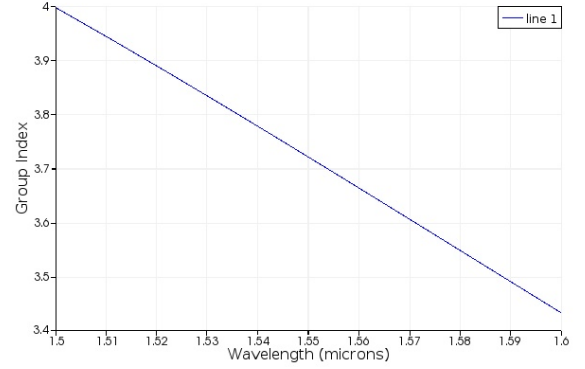


Fig. 8: Group Index (n_g) for quasi-TM mode

based on a second order polynomial fit. We used the Lumerical scripting tool to obtain the fit parameters.

For the quasi-TE mode the effective index approximates to:

$$n_{eff} = 2.444350 - 1.12728(\lambda - 1.55) - 0.0334863(\lambda - 1.55)^2 \quad (10)$$

For the quasi-TM mode the effective index approximates to:

$$n_{eff} = 1.77142 - 1.25746(\lambda - 1.55) + 1.83385(\lambda - 1.55)^2 \quad (11)$$

Fig. 9 and fig. 10 provides the curve fit plot we obtained for both the quasi-TE and quasi-TM mode of the waveguide. In the following section, the responses of the quasi-TE and quasi-TM mode MZI design would be obtained. In the plots we see a single curve instead of two because the curve fits so accurate that the two lines overlapped.

D. Circuit Simulation

Lumerical Interconnect was used for circuit simulation of the Mach Zehnder Interferometer to obtain the response for different path length difference ΔL in both the quasi-TE and quasi-TM mode. The schematic of the circuit as drawn in Interconnect is shown in fig. 11 and fig. 12. For the simulations of TE mode MZI, we used the TE mode fiber grating couplers as well as the Y-branch, provided in the compact model library. In the TM mode MZI, we used the TM mode fiber grating couplers. For the arms of the interferometers, we used Lumerical MODE solutions simulated data for the straight

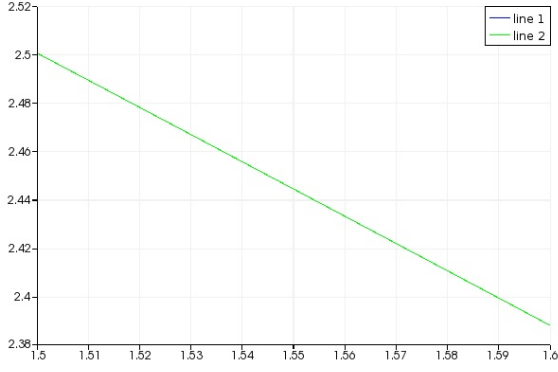


Fig. 9: A second order polynomial curve fit for quasi-TE mode

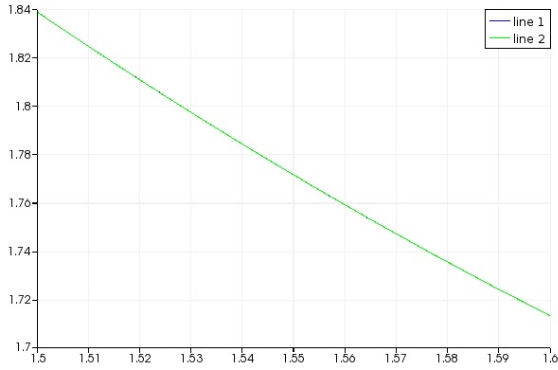


Fig. 10: A second order polynomial curve fit for quasi-TM mode

waveguide as obtained in the previous section. One important thing to note is that, for accurate simulations it is always an advantage to consider bent waveguides but since in the layout of our design there are no 90 degrees sharp bends but nearly circular ones at certain radius (i.e. $5\mu m$ for the quasi-TE mode and $33\mu m$ for the quasi-TM mode), we choose to simulate with the straight waveguide.

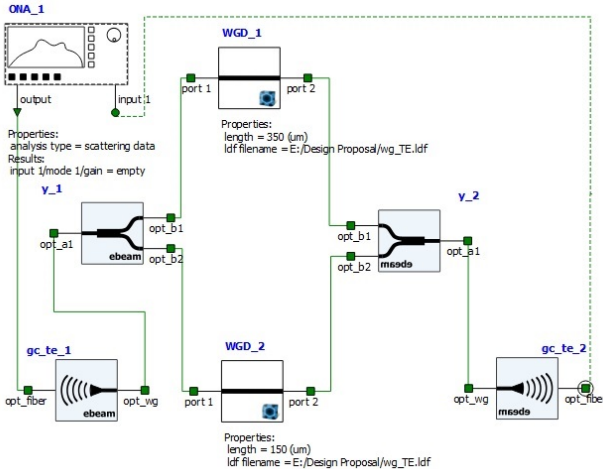


Fig. 11: TE mode MZI circuit

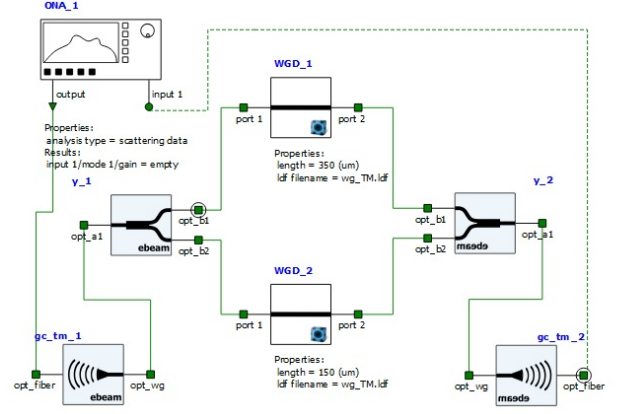


Fig. 12: TM mode MZI circuit

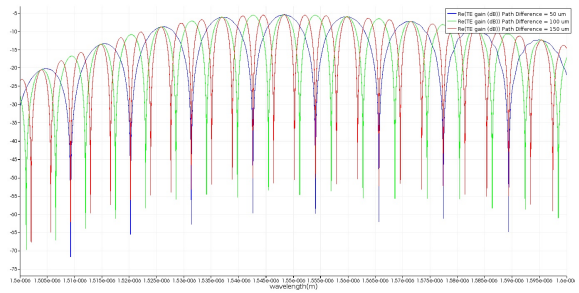


Fig. 13: Simulated gain response of three MZI designs for quasi-TE mode: $\Delta L = 50\mu m$, $\Delta L = 100\mu m$, $\Delta L = 150\mu m$

We also considered some extra losses in our models for both quasi-TE and TM modes of the circuit. The value of the extra losses for the waveguides were calculated from the following equation:

$$ExtraLoss[dB] = L * A_{Optical} \quad (12)$$

where L denotes the length of the waveguide and $A_{Optical}$ is the optical loss. A value of 5.9dB/cm was taken for the quasi-TE mode whereas a value of 1.2dB/cm was taken for the quasi-TM mode. TM waveguides have lower loss since the E-field interacts less with the sidewalls than in the TE case. There is also less back-scattering in the TM case, hence the optical spectra are "cleaner". But TM waveguides require a larger bend radius.

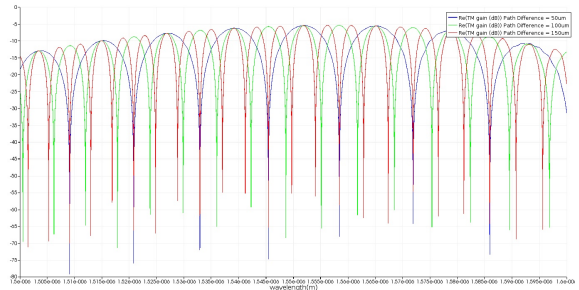


Fig. 14: Simulated gain response of three MZI designs for quasi-TM mode: $\Delta L = 50\mu m$, $\Delta L = 100\mu m$, $\Delta L = 150\mu m$

Device ID	$L_1[\mu m]$	$L_2[\mu m]$	$\Delta L[\mu m]$	$FSR[nm]$
MZI1	160	210	50	11.633
MZI2	100	200	100	5.675
MZI3	155	305	150	3.722
MZI4	150	350	200	2.842

TABLE I: MZI Design Parameters [quasi-TE Mode]

Device ID	$L_1[\mu m]$	$L_2[\mu m]$	$\Delta L[\mu m]$	$FSR[nm]$
MZI5	160	210	50	12.919
MZI6	100	200	100	6.314
MZI7	155	305	150	4.193
MZI8	150	350	200	3.187

TABLE II: MZI Design Parameters [quasi-TM Mode]

Table I and II provides the design parameters for the various MZIs we have designed using Interconnect in both quasi-TE and TE mode. Only one parameter namely the path length difference (ΔL) between both the arms (L_1 and L_2) of the Mach-Zehnder Interferometer has been varied. Simultaneously, the FSR was also noted for each configuration as well. Figures 13 and 14 illustrate the gain responses of those interferometers. The results show the effect of the path length difference (ΔL), where shorter differences gives few peak responses or large FSR. The FSR is reduced as the (ΔL) increase, which is evident from eqn.(9) derived in the earlier section. The FSR obtained for both quasi-TE and TM modes were different.

IV. FABRICATION

A. GDS Layout Description

The dimension of the layout was $605\mu m$ (width) by $410\mu m$ (height). Fig. 12 depicts the layout which was submitted for fabrication. A total of ten structures were submitted out of which two were de-embedding structures i.e. grating couplers. The de-embedding structures were placed close to the MZI designs so that the variations which were there due to manufacturing limitations may be minimized. The rationale behind putting such structures was to calibrate the measurement system insertion loss. As seen from the figure, the lower row consisted of various quasi-TE mode MZI designs unlike the top row where only quasi-TM mode MZIs were kept. The path length difference (ΔL) were varied from 50 microns up to 200 microns across both the quasi-TE and TM mode MZIs. The grating coupler for any particular design was kept at a distance of $127\mu m$ from each other. This was done for ease of measurement and also since we will be going for a single etch design for our waveguides in contrast to a partial etch design. Moreover, the grating couplers for the quasi-TE mode MZI designs were kept facing left unlike the quasi-TM mode designs which were faced to the right for the ease of measurement.

Since the measurement instrument had to be about rotated 180° for effective quasi-TM mode MZI measurements in comparison to the quasi-TE mode MZIs, it was better to rotate the grating couplers itself on the layout. This was easy,

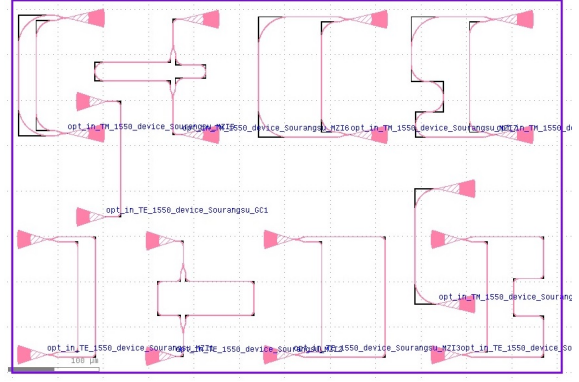


Fig. 15: GDS Layout

efficient and saved a lot of work hours and effort towards measurement. The design meets all the manufacturability design rules (DRC) and the minimum feature size for any component on the layout was greater than $60nm$. Special precautions were taken to check that all the waveguides were connected with no broken or unmatched regions in between. There were no sharp 90° bends i.e. all the waveguide paths were converted to waveguides with appropriate bend radius. The structures were designed in such a way that they will have low optical loss i.e. there were sufficient space (approx. $10\mu m$) between waveguides to avoid optical cross-talk. It was also checked that all the structures were on the correct layer. The measurement labels were unique and all the devices had the correct text label for automated measurements.

B. Fabrication Description

The devices were fabricated using $100keV$ Electron Beam Lithography [13]. The fabrication used silicon-on-insulator wafer with $220nm$ thick silicon on $3\mu m$ thick silicon dioxide. The substrates were $25mm$ squares diced from $150mm$ wafers. After a solvent rinse and hot-plate dehydration bake, hydrogen silsesquioxane resist (HSQ, Dow-Corning XP-1541-006) was spin-coated at $4000rpm$, then hotplate baked at $80^\circ C$ for 4 minutes. Electron beam lithography was performed using a JEOL JBX-6300FS system operated at $100keV$ energy, $8nA$ beam current, and $500\mu m$ exposure field size. The machine grid used for shape placement was $1nm$, while the beam stepping grid, the spacing between dwell points during the shape writing, was $6nm$. An exposure dose of $2800\mu C/cm^2$ was used. The resist was developed by immersion in 25% tetramethylammonium hydroxide for 4 minutes, followed by a flowing deionized water rinse for 60s, an isopropanol rinse for 10s, and then blown dry with nitrogen [15][16]. The silicon was removed from unexposed areas using inductively coupled plasma etching in an Oxford Plasmalab System 100, with a chlorine gas flow of $20sccm$, pressure of $12mT$, ICP power of $800W$, bias power of $40W$, and a platen temperature of $20^\circ C$, resulting in a bias voltage of $185V$. During etching, chips were mounted on a $100mm$ silicon carrier wafer using perfluoropolyether vacuum oil.

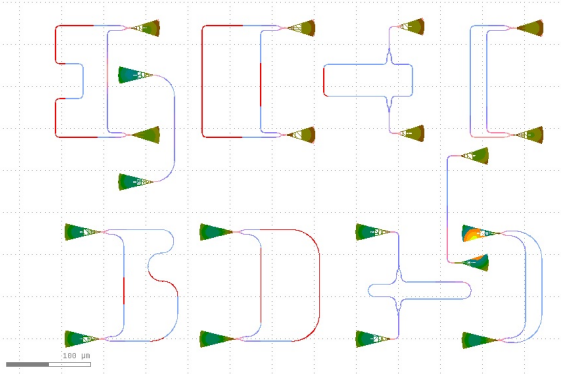


Fig. 16: The layout after fracturing and dosage correction

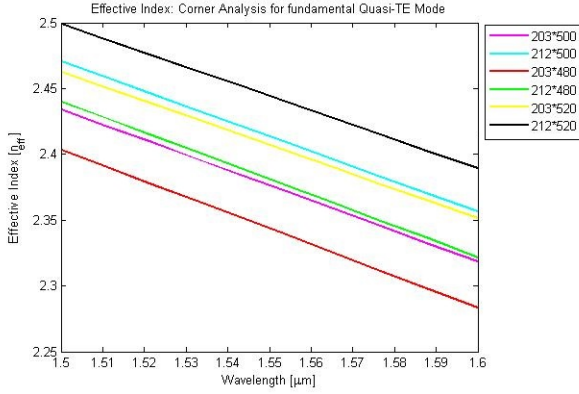


Fig. 17: Corner Analysis of Effective Index for the fundamental Quasi-TE Mode

V. MANUFACTURING CHALLENGES

In this section, we discuss the impact of manufacturing variability of silicon photonics. Photonic integrated circuits often require that components be precisely matched in terms of the central wavelength. This requires that the waveguide propagation constants are well-matched. Understanding the fabrication variability is critical to developing strategies for system implementation and for determining the cost implications for such compensation strategies. These variations appear from wafer to wafer, as well as within a single photonic integrated circuit. The dominant manufacturing parameter that results in optical component and circuit variation has been identified to be the top silicon thickness variation. Another manufacturing parameter that results in optical component and circuit variation is the variation in the feature size. When a waveguide is drawn to be 500nm, it is quite uncertain as to what the resulting width might be.

It has been seen that the variation and feature size is also dependent on the fabrication steps. First, we have the resist, which can vary in thickness and sensitivity, and is also affected by the age of the resist. Next, is the variation in the exposure of the resist, which in the case of electron beam lithography are both the dosage and the position of the electron beam. The beam position can vary due to the noise in the system or due to the drawing of the mask and how it has been fractured into pixels. Then there is the development process,

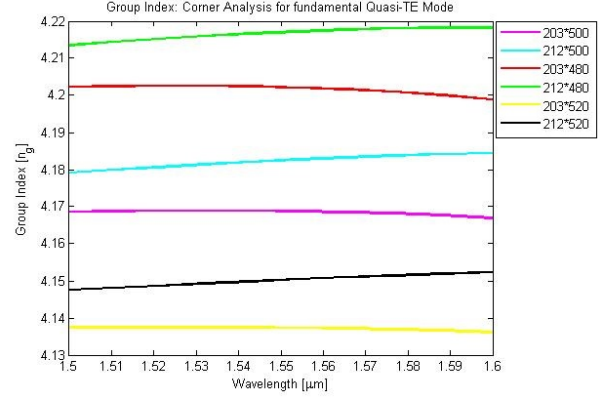


Fig. 18: Corner Analysis of Group Index for the fundamental Quasi-TE Mode

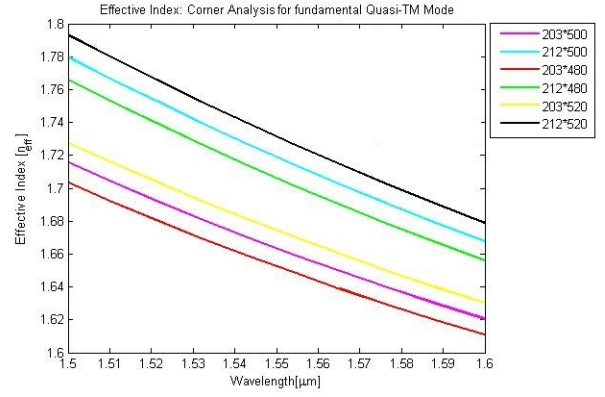


Fig. 19: Corner Analysis of Effective Index for the fundamental Quasi-TM Mode

which is sensitive to the development time and chemical aging. Finally, we have the etching process, which depends on the etch chamber conditions, namely how clean it is, gas concentrations, etching time, and so on. All these fabrication process variations lead to feature size variations. The chip was measured and mapped out the SOI thickness (Si and BOX) on the actual chips prior to fabrication. A single-point ellipsometer measurement was done in the middle, and they agreed with astonishingly close numbers. In conclusion, we can say that the chips are thinner than expected.

A. Corner Analysis

We used a technique called corner analysis to predict the variations in device and circuit performance. Corner analysis is a simple design of experiment technique that considers typical process variations. In photonics, we consider devices that require a single etch step, such a strip waveguides. We considered process variations in two dimensions, namely the thickness and width variations. The nominal design is a waveguide with geometry of 500nm by 220nm. The same corner analysis cases were taken up for both the quasi-TE and quasi-TM mode.

First, we consider the height. The design target is 220 nanometers. But the wafers we had are specified to be

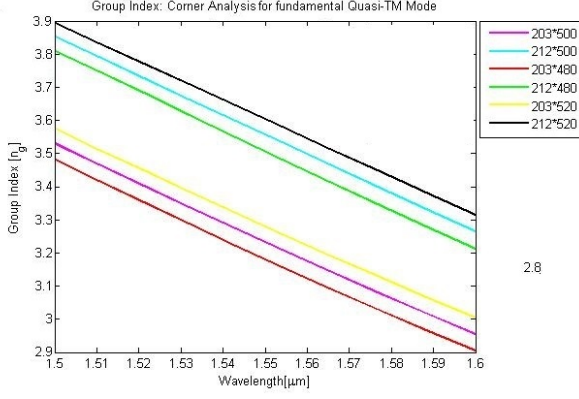


Fig. 20: Corner Analysis of Group Index for the fundamental Quasi-TM Mode

$\Delta L[\mu m]$	$FSR_{Min}[nm]$	$FSR_{Max}[nm]$
50	11.253	11.784
100	5.616	5.695
150	3.712	3.792
200	2.211	2.787

TABLE III: Corner Analysis: FSR [quasi-TE Mode]

$\Delta L[\mu m]$	$FSR_{Min}[nm]$	$FSR_{Max}[nm]$
50	11.871	14.111
100	5.787	7.606
150	4.057	5.103
200	2.915	3.863

TABLE IV: Corner Analysis: FSR [quasi-TM Mode]

204.2nm. Hence, on the y-axis, we took a range of 203nm to 212nm. For the width, we had a target of 500 nanometers. We used a range of minus 20 to plus 20 nanometers i.e. 480nm to 520nm. Fig. 17 and Fig.18 shows the corner analysis plots for the quasi-TE mode. From the plots we see that the effective index ranges from 2.349 to 2.452 and the group index ranges from 4.137 to 4.218. Similarly, Fig. 17 and Fig.18 depicts the corresponding plots for the quasi-TM mode. From the figures, we see that at 1,550nm that the effective index ranges from 1.736 to 1.652 and the group index ranges from 3.176 to 3.622 for the quasi-TM mode. From the corner analysis results, it is pretty evident that the effective index and the group index values varies from the nominal simulation values by a greater amount for the quasi-TM mode than for the quasi-TE mode. The FSRs extracted for each of the path length difference (ΔL) used in our MZI designs had been provided in Table 4 and Table 5 for each of the modes. Since, our nominal design considers a waveguide geometry of 220nm (height) X 500nm (width), the simulated results is not expected to lie within the range of the corner analysis but close to it. In contrast, the fabricated MZI designs should have the waveguide performance somewhere within this range.

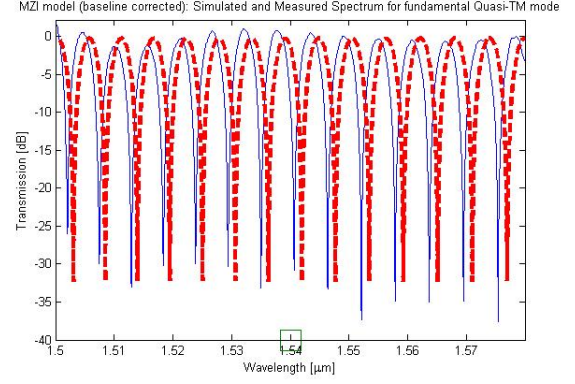


Fig. 21: Simulated and Measured MZI spectrum for fundamental Quasi TE-Mode with $\Delta L = 100\mu m$

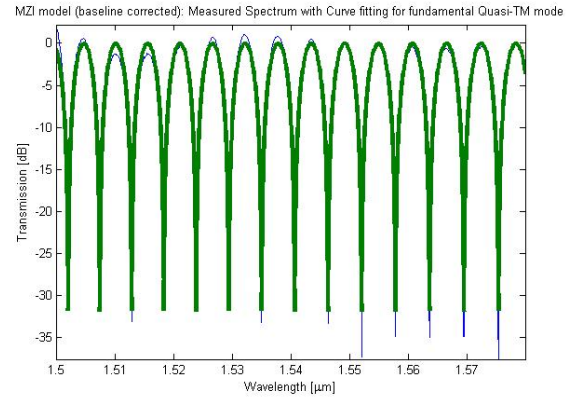


Fig. 22: Measured MZI spectrum with Curve Fitting for fundamental Quasi TE-Mode with $\Delta L = 100\mu m$

VI. MEASUREMENT

A. Measurement Description

To characterize the devices, a custom-built automated test setup [1] with automated control software written in Python was used [14]. An Agilent 81600B tunable laser was used as the input source and Agilent 81635A optical power sensors as the output detectors. The wavelength was swept from 1500 to 1600 nm in 10 pm steps. A polarization maintaining (PM) fibre was used to maintain the polarization state of the light, to couple the TE polarization into the grating couplers [9]. A 90 rotation was used to inject light into the TM grating couplers [4][8]. A polarization maintaining fibre array was used to couple light in/out of the chip [10][16].

B. Curve Fitting and Extracted Parameters

The experimental MZI spectrums we obtained for both the quasi-TE and quasi-TM mode MZI designs were curve fitted with one of the curve-fitting techniques to extract important parameters like the group index and free spectral range(FSR). However, before any of the curve fitting techniques were employed, we applied a baseline correction to flatten the MZI spectrum. Fig. 21 and fig. 22 shows the baseline corrected plots of the measured MZI spectrum which is first compared with our nominal simulation in the first plot followed by

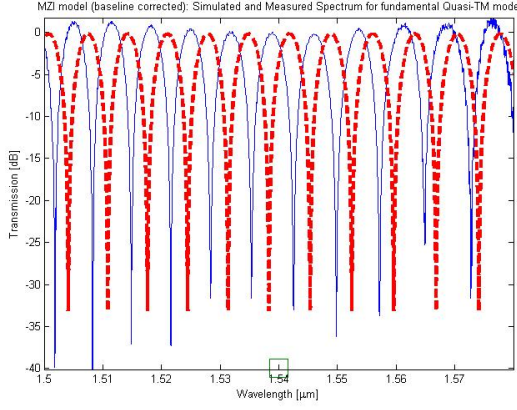


Fig. 23: Simulated and Measured MZI spectrum for fundamental Quasi TM-Mode with $\Delta L = 100\mu m$

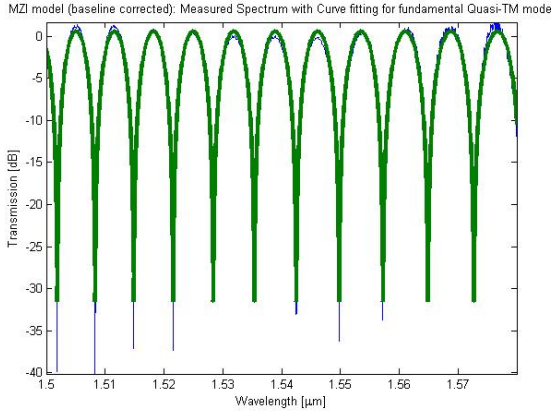


Fig. 24: Measured MZI spectrum with Curve Fitting for fundamental Quasi TM-Mode with $\Delta L = 100\mu m$

$\Delta L[\mu m]$	n_g	$FSR[nm]$
50	4.169	11.591
100	4.193	5.633
150	4.188	3.745
200	4.196	2.527

TABLE V: Extracted Parameters [quasi-TE Mode]

the curve fitting plot for the quasi-TE mode. Consequently, in the following two figures i.e. fig. 23 and fig. 24 the respective spectrum is shown for the quasi-TM mode. The path length difference (ΔL) for both the modes is considered to be $100\mu m$. Similar, plots was obtained when the same curve fitting techniques was applied on different MZI designs with varying (ΔL). Table 6 shows the parameters which were extracted after the curve fitting was applied on each of our MZI designs.

VII. SIMULATION V/S MEASUREMENT

In this section we bring out the comparison of the simulation versus the measurement data. The plots of the effective index (n_{eff}) and the group index (n_g) against the wavelength for the quasi-TE mode is shown in fig. 25 and fig. 26. Fig. 27 and

$\Delta L[\mu m]$	n_g	$FSR[nm]$
50	3.282	12.425
100	3.337	6.717
150	3.521	4.553
200	3.526	3.051

TABLE VI: Extracted Parameters [quasi-TM Mode]

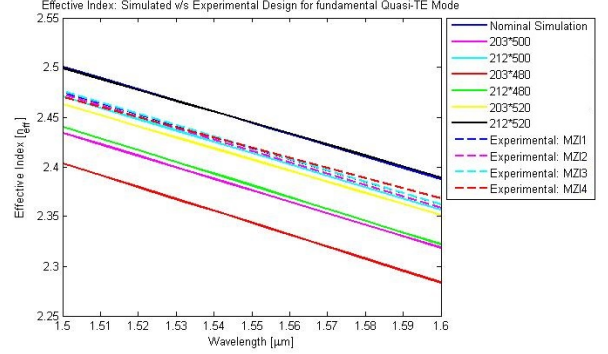


Fig. 25: Comparative Analysis of Effective Index for both Simulated and Experimental designs for the fundamental Quasi-TE Mode

fig. 28 shows the same for the quasi-TM mode. The value of the parameters n_{eff} and n_g for our nominal simulated design was nowhere close to the corner analysis that we did for the quasi-TM mode case. In contrast the offset in the parameter values was less for the quasi-TE mode.

However, the plots still provide evidence to the fact that the measured data that we got from our experimental MZI designs lies well within the corner analysis which we had done for both the quasi-TE and quasi-TM mode with some minor exceptions (the value of n_{eff} for the quasi-TM mode MZI design with $\Delta L = 100\mu m$ at 1550nm was outside the corner analysis range by a small extent while the n_g value for that same device was well with the range). Even though, our simulated nominal design which had dimensions of 220nm by 500nm was not quite within the range of our corner analysis owing to the fact that the chip we received for fabrication was

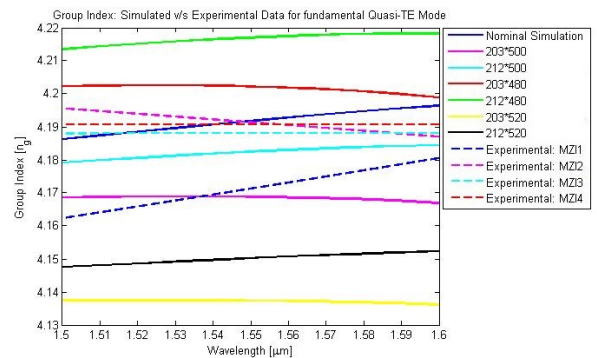


Fig. 26: Comparative Analysis of Group Index for both Simulated and Experimental designs for the fundamental Quasi-TE Mode

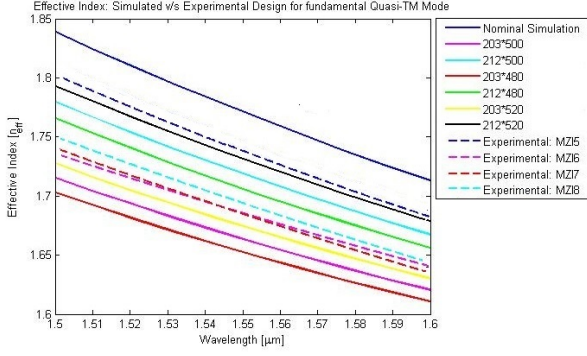


Fig. 27: Comparative Analysis of Effective Index for both Simulated and Experimental designs for the fundamental Quasi-TM Mode

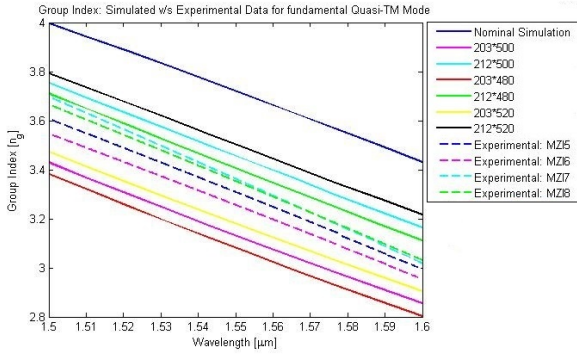


Fig. 28: Comparative Analysis of Group Index for both Simulated and Experimental designs for the fundamental Quasi-TM Mode

thinner than the conventional ones, the extracted parameters from the simulated as well as the measured data were quite close.

VIII. CONCLUSION

In conclusion, we can say that our theoretical study of the Mach Zehnder Interferometer (MZI), the simulations we made taking into account the manufacturing challenges to predict the variation in the performance of our fabricated devices and the measurement results we got from the fabrication were all in good agreement with each other considering the fact that the chip we received for fabrication was thinner than regular ones. The offset in the parameters were not that much. However, modelling the right waveguide geometry i.e. width and height from the measurement data of our fabricated devices with the extracted parameters does not yield good results. As far as we have seen, we haven't been able to achieve any unique "solution", to be sure that we know for sure the size of the waveguide.

ACKNOWLEDGMENT

We acknowledge the edX UBCx Silicon Photonics Design, Fabrication and Data Analysis course, which is supported by the Natural Sciences and Engineering Research Council

of Canada (NSERC) Silicon Electronic-Photonic Integrated Circuits (SiEPIC) Program. The devices were fabricated by Richard Bojko at the University of Washington Washington Nanofabrication Facility, part of the National Science Foundations National Nanotechnology Infrastructure Network (NNIN). Zeqin Lu performed the measurements at The University of British Columbia. We acknowledge Lumerical Solutions, Inc., Mathworks, Mentor Graphics, Python, and KLayout for the design software. We would like to thank Dr. Lukas Chrostowski as well as all the peers who had motivated and helped to finish this project by giving their valuable suggestions and advice.

REFERENCES

- [1] L. Chrostowski and M. Hochberg, *Silicon Photonics Design: From Devices to Systems*. Cambridge University Press, 2015.
- [2] <https://www.rp-photonics.com/interferometers.html>
- [3] Hae Young Choi, Myoung Jin Kim, and Byeong Ha Lee. "All-fiber Mach-Zehnder type interferometers formed in photonic crystal fiber." *Optics Express* 15.9 (2007): 5711-5720.
- [4] Arpan Deyasi, Sourangsu Banerji, Sayan Bose, and Abhishek Halder. "Analytical Computation of Band Structure of 1D Photonic Crystal Under Normal Incidence of Electromagnetic Wave." In *Computational Advancement in Communication Circuits and Systems*, pp. 331-338. Springer India, 2015.
- [5] Sourangsu, Abhishek Halder, Arpan Deyasi, and Sayan Bose. "Comparative study of density of states of 1D photonic crystal for different polarization conditions of incident wave." In *Electronics, Communication and Instrumentation (ICECI), 2014 International Conference on*, pp. 1-4. IEEE, 2014.
- [6] Sourangsu Banerji, and Arpan Deyasi. "Application of group theory in transfer matrix technique for band structure calculation in 1D photonic crystal." In *Computer, Communication and Control (IC4), 2015 International Conference on*, pp. 1-5. IEEE, 2015.
- [7] Jos Mora, Beatriz Ortega, Antonio Dez, Jos Luis Cruz, Miguel V. Andrs, Jos Capmany, and Daniel Pastor.. "Photonic microwave tunable single-bandpass filter based on a Mach-Zehnder interferometer." *Journal of lightwave technology* 24.7 (2006): 2500.
- [8] Marin Soljacic, Shanhui Fan, Mihai Ibanescu, Steven G. Johnson, and John D. Joannopoulos. "Mach-Zehnder interferometer using photonic band gap crystals." U.S. Patent 6,917,431, issued July 12, 2005.
- [9] Edward D. Palik, *Handbook of optical constants of solids*. Vol. 3. Academic press, 1998.
- [10] Sourangsu Banerji, To Study the Effect of Grating Length on Propagating Modes in Bragg Filters with AlXGa1-XN/GaN Material Composition. arXiv preprint arXiv:1312.4762 (2013).
- [11] Sourangsu Banerji, Group Theoretic Approach To Study Transfer Matrix Method In One-Dimensional Photonic Crystals.
- [12] A. Deyasi, S. Banerji, A. Halder, and S. Bose, (2014, September). Theoretical Investigation on Photonic Bandgap Tailoring in One-Dimensional Photonic Crystal Using Different Numerical Methods. In *Devices, Circuits and Communications (ICDCCom), 2014 International Conference on* (pp. 1-6). IEEE.
- [13] R. J. Bojko, J. Li, L. He, T. Baehr-Jones, M. Hochberg, and Y. Aida, "Electron beam lithography writing strategies for low loss, high confinement silicon optical waveguides," *J. Vacuum Sci. Technol. B* 29, 06F309 (2011)
- [14] <http://siepic.ubc.ca/probestation>, using Python code developed by Michael Caverley.
- [15] Yun Wang, Xu Wang, Jonas Flueckiger, Han Yun, Wei Shi, Richard Bojko, Nicolas A. F. Jaeger, Lukas Chrostowski, "Focusing sub-wavelength grating couplers with low back reflections for rapid prototyping of silicon photonic circuits", *Optics Express* Vol. 22, Issue 17, pp. 20652-20662 (2014) doi: 10.1364/OE.22.020652
- [16] www.plcconnections.com, PLC Connections, Columbus, OH.